

## Sea Ice

# Sea Ice

Third Edition

EDITED BY

**David N. Thomas**

School of Ocean Sciences, Bangor University, UK

and

Marine Research Center, Finnish Environment Institute (SYKE), Helsinki, Finland

**WILEY** Blackwell

This edition first published 2017 © 2003, 2010, 2017 by John Wiley & Sons, Ltd

*Registered office:* John Wiley & Sons, Ltd, The Atrium, Southern Gate, Chichester, West Sussex, PO19 8SQ, UK

*Editorial offices:* 9600 Garsington Road, Oxford, OX4 2DQ, UK

The Atrium, Southern Gate, Chichester, West Sussex, PO19 8SQ, UK

111 River Street, Hoboken, NJ 07030-5774, USA

For details of our global editorial offices, for customer services and for information about how to apply for permission to reuse the copyright material in this book please see our website at [www.wiley.com/wiley-blackwell](http://www.wiley.com/wiley-blackwell).

The right of the author to be identified as the author of this work has been asserted in accordance with the UK Copyright, Designs and Patents Act 1988.

All rights reserved. No part of this publication may be reproduced, stored in a retrieval system, or transmitted, in any form or by any means, electronic, mechanical, photocopying, recording or otherwise, except as permitted by the UK Copyright, Designs and Patents Act 1988, without the prior permission of the publisher.

Designations used by companies to distinguish their products are often claimed as trademarks. All brand names and product names used in this book are trade names, service marks, trademarks or registered trademarks of their respective owners. The publisher is not associated with any product or vendor mentioned in this book.

**Limit of Liability/Disclaimer of Warranty:** While the publisher and author(s) have used their best efforts in preparing this book, they make no representations or warranties with respect to the accuracy or completeness of the contents of this book and specifically disclaim any implied warranties of merchantability or fitness for a particular purpose. It is sold on the understanding that the publisher is not engaged in rendering professional services and neither the publisher nor the author shall be liable for damages arising herefrom. If professional advice or other expert assistance is required, the services of a competent professional should be sought.

*Library of Congress Cataloging-in-Publication Data*

Names: Thomas, David N. (David Neville), 1962- editor.

Title: Sea ice / edited by David N. Thomas.

Description: Third edition | Chichester, UK ; Hoboken, NJ : John Wiley & Sons, 2017. | Includes index.

Identifiers: LCCN 2016031586 | ISBN 9781118778388 (cloth) | ISBN 9781118778357 (epub)

Subjects: LCSH: Sea ice.

Classification: LCC GB2403.2 .S43 2017 | DDC 551.34/3 – dc23 LC record available at <https://lcn.loc.gov/2016031586>

A catalogue record for this book is available from the British Library.

Wiley also publishes its books in a variety of electronic formats. Some content that appears in print may not be available in electronic books.

Cover image: Courtesy of David N. Thomas

Set in 8.5/12pt, MeridienLTStd by SPi Global, Chennai, India.

## CHAPTER 9

# Methods of satellite remote sensing of sea ice

Gunnar Spreen<sup>1\*</sup> and Stefan Kern<sup>2</sup>

<sup>1</sup>Norwegian Polar Institute, Tromsø, Norway

<sup>2</sup>University of Hamburg, Integrated Climate Data Centre – ICDC, Hamburg, Germany

## 9.1 Introduction

Sea ice floats on the polar and sub-polar oceans. It covers on average between 17 million and 27 million square kilometres of the Earth (Parkinson, 2014). Such a vast area can only be monitored using satellite remote sensing. Every acquisition of information without physical contact can be called remote sensing, e.g. taking a photo. Hence, satellite remote sensing in the visible part of the electromagnetic (EM) spectrum can be compared with taking a photo from space. This chapter considers remote sensing over a wider range of the EM spectrum and will focus on the technical aspects of satellite sea ice remote sensing. The results are shown and interpreted in several other chapters in this book.

The Intergovernmental Panel on Climate Change (IPCC) Fifth Assessment Report (IPCC, 2013) gives an impression of how important remote sensing is for current sea ice research. In the executive summary of the chapter on ‘Cryosphere’, five important findings regarding changes in sea ice are highlighted. Four out of these five findings are based on satellite observations, namely since 1979: (1) Arctic sea ice extent decreased; (2) Arctic perennial and multi-year ice decreased; (3) the period of surface melt on Arctic perennial ice lengthened; and (4) Antarctic sea ice extent increased, however, with strong regional differences. Only the fifth point, the decrease of Arctic sea ice thickness, is based on a combination of submarine, airborne and satellite observations due to the short length of the satellite ice thickness record. Without satellites we would know much less and with lower confidence about sea ice and the climate in the polar regions.

### 9.1.1 Basic concepts and principles

Satellite sensors can obtain a vast number of observations compared with ground-based measurements. A single observation or image does not tell too much about the spatiotemporal development of the sea ice. One needs a series of images ideally of the same area at different times of the seasonal cycle of the sea ice. This is realized by using polar-orbiting satellites, which complete one orbit around the Earth in typically around 100 minutes. If the satellite sensor offers a swath width (Figure 9.1) of more than 1500 km, the complete global sea ice cover can be observed on a daily basis leaving only small, unobserved holes at the poles.

During polar night, taking a photo is difficult because the scene needs to be illuminated by sunlight. Also clouds may obscure the scene, rendering observations taken in the visible portion of the EM spectrum useless for sea ice research. Sensor technology has advanced very much from just taking a single photo, however. Satellite remote sensing of sea ice is carried out in the visible, infrared and microwave portions of the EM spectrum (Figure 9.2). This permits remote sensing throughout the polar night and mitigation of the influence of clouds and other atmospheric constituents.

Depending on the frequency range, one obtains a picture of the surface brightness which depends on solar illumination for the visible portion of the EM spectrum (Section 9.5). The measured intensity in the infrared and microwave frequency range depends on the capabilities of the sea ice to emit EM radiation as a function of its physical temperature and emissivity, which is determined by geophysical quantities such as salinity,

\*Present address: Institute of Environmental Physics, University of Bremen, Otto-Hahn-Allee 1, D-28359 Bremen, Germany.

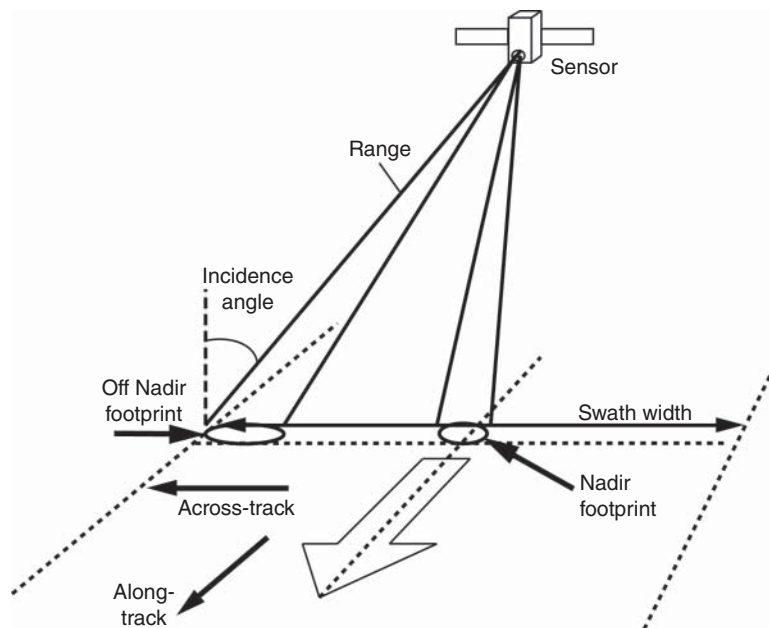


**Figure 9.1** Schematic of a typical satellite viewing geometry and important definitions. Every sensor, however, has its specific geometry. For example, altimeters do not scan and only observe at nadir; while radiometers such as the special sensor microwave imager (SSM/I) scan elliptically (not along a line) under a constant incidence angle, have a constant footprint size but no nadir observations.

roughness, porosity and air content (Chapter 1). Such sensors are called (spectro-) radiometers (Section 9.2).

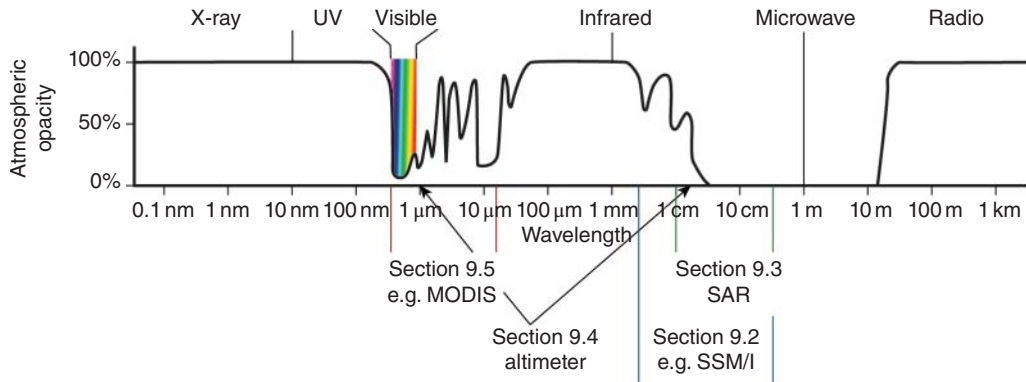
Other sensors actively emit EM radiation and measure the amount of this radiation scattered back to the sensor from the sea ice. This backscatter can be translated into an image of the backscattering properties of the sea ice. These properties depend on the internal and surface structure of the sea ice (see Chapter 1). Such sensors operate in the microwave frequency range and are called scatterometers (Section 9.2) and synthetic aperture radar (SAR; Section 9.3). Other sensors measure the runtime of an emitted EM pulse between the sensor and the surface. The runtime can be translated into the distance between the satellite sensor and the surface. Such sensors are called altimeters (Section 9.4).

Figure 9.1 shows a schematic of the typical geometry of how a satellite sensor sees the Earth. The size of the sensor footprint, i.e. the area illuminated or sensed by the sensor at the surface, determines the spatial resolution of the observations. Depending on the type of sensor, footprint sizes vary between a few metres (visible and SAR sensors) to tens of kilometres (radiometers). The swath width determines how much of the Earth's surface is observed during one satellite

overflight, i.e. one orbit. The swath width varies between point measurements of a few tens of metres (laser altimeter) and about 2500 km (some optical sensors and radiometers). Depending on the swath width, it can take between 1 day and several months until the polar regions are covered by observations from a particular satellite sensor (compare 1 day of ICESat observations in Figure 9.4f with the 1 day coverage of other sensors in Figure 9.4a–d).

### 9.1.2 Short overview of important missions for sea ice remote sensing

The first images of sea ice from satellites reach as far back as 1964 (Meier et al., 2013). A milestone for sea ice remote sensing, however, was the launch of the Nimbus-7 satellite carrying the scanning multichannel microwave radiometer (SMMR) in October 1978. Measurements from this sensor together with its successors, the special sensor microwave imager (SSM/I) and the special sensor microwave imager/sounder (SSMIS) now form the basis of the more than 35-year-long time series of daily, global sea ice observations. The primary sea ice parameter obtained from these sensors is the sea ice area (Section 9.2.2), but other applications exist



**Figure 9.2** The electromagnetic spectrum and atmospheric opacity. Satellite remote sensing focuses on the window wavelength marked at the bottom with the sections in which the respective sensors are discussed.

(Sections 9.2.3–9.2.6). This sea ice area time series is one of the longest satellite records existing today and, as mentioned before, enabled us to monitor the unprecedented change in Arctic sea ice cover during recent decades. With a gap in observations between 1977 and 1978 and lower spatial and temporal resolution, this time series can even be extended back until December 1972, when the electrically scanning microwave radiometer (ESMR) on Nimbus-5 was launched.

Another milestone in sea ice remote sensing was reached when the first map of the Arctic Ocean sea ice thickness distribution from satellite altimetry was obtained (Laxon et al., 2003). Before this, only the spatial dimension of different sea ice variables could be obtained. The utilization of altimeters on the ERS1/2, Envisat, ICESat, and CryoSat-2 satellites for ice thickness retrieval added the third dimension to sea ice observations from space.

There are many more achievements in both satellite sensor technology and algorithm development, which cannot all be listed here. Some of the most important aspects will be discussed throughout the course of this chapter.

### 9.1.3 The EM spectrum

The most basic concept of satellite remote sensing is to measure EM radiation with a sensor in space (Campbell & Wynne, 2011). Figure 9.2 shows the EM spectrum and the wavelength ranges relevant for remote sensing of sea ice (including the sections they are discussed in). Sea ice remote sensing concentrates on the atmospheric windows in the visible, infrared and microwave portion of the EM spectrum. Only in these wavelength bands

is the atmosphere (partly) transparent for EM radiation (Figure 9.2). There are two fundamentally different principles of remote sensing:

- Active sensors send out an EM signal themselves and record the reflected or backscattered radiation from the Earth's surface. Examples are the QuikSCAT scatterometer (Section 9.2) and all SAR sensors (Section 9.3). These measure the backscattered microwave radiation from the sea ice under typical incident angles between 20° and 55°. Other examples are the laser and radar altimeters (Section 9.4). These measure the EM signal runtime and thereby the distance between the sensor and the Earth's surface.
- The second group of sensors observes the Earth in a passive way without sending out a signal themselves. Here again **two different principles can be discriminated**: either the sensor measures the EM radiation from the Sun after it was reflected by the Earth's surface (this is the case for observations within the visible and near-infrared bandwidth and only possible in daylight; Section 9.5) or the sensor measures the EM radiation emitted by the Earth's surface itself. This is the case for the thermal-infrared and microwave wavelengths (Sections 9.2 and 9.5).

Figure 9.3 shows how these different measurement principles can be explained. Following Planck's law for black body radiators, the Earth is not emitting any radiation in the visible and near-infrared EM spectrum and therefore only reflected radiation from the Sun can be observed.

The Earth shows its maximum EM emission in the thermal-infrared spectrum, and for cloud-free conditions the physical Earth surface temperature can

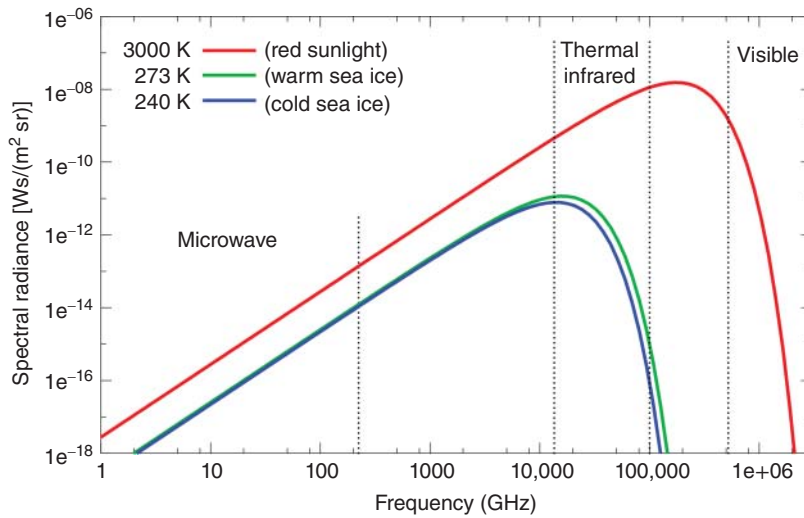


**Figure 9.3** Emitted spectral radiance of a black body radiator following Planck's law. The radiation of black bodies with 240, 273 and 3000 K temperature is shown representing cold and warm sea ice surfaces, and the red part of the Sun's spectrum.

be measured in this EM range. The microwave EM range is well suited for spaceborne remote sensing, as microwave radiation can **penetrate clouds**. The emitted Earth radiation in the microwave range, however, is more than three orders of magnitudes lower than in the thermal infrared range (mind the exponential scale in Figure 9.3). For the radiation emitted by sea ice at microwave frequencies, the idealized black body radiator is not a good approximation. For the microwave brightness temperature,  $T_B = \epsilon T$ , measured by a radiometer, the emissivity  $\epsilon$  is not close to 1 (as it would be for a black body) but highly variable. Therefore radiometers mainly measure the emissivity  $\epsilon$  in the microwave range and only to a second degree the physical temperature  $T$ .

### 9.1.4 Scattering mechanisms

How much energy is recorded by a satellite sensor is strongly determined by scattering of the EM waves in the atmosphere and on the ground. In the atmosphere aerosols, water vapour, and hydrometeors like rain, snow and cloud liquid water are the main sources of scatter. Depending on the ratio between EM wavelength  $\lambda$  and the radius  $r$  of these scattering particles, different scattering mechanisms have to be discriminated, e.g. Rayleigh scattering for  $r \ll \lambda$  or Mie scattering for  $r \approx \lambda/2\pi$ . In addition to the size, the shape and dielectric properties of the particles also influence the

scattering. Atmospheric scattering can be complex and is not discussed further here.

For EM scattering on the ground, two main processes can be discriminated: surface and volume scattering. Besides the dielectric properties of the surface material, the surface roughness is a key factor for the EM backscatter. A very flat or specular surface will only reflect EM radiation back to the sensor if the sensor's line of sight and the surface are perpendicular, as for a mirror. This is only the case for flat surfaces and nadir-looking sensors, or if the surface is tilted towards the sensor as is the case with mountains or, in our case, sea ice pressure ridges and water surface waves. Otherwise, for specular surfaces, all radiation will be reflected away from the sensor and the surface will have a very low backscatter value. Low backscatter is often displayed black or with dark colours in a satellite image. A rough surface will scatter a fraction of the incoming EM radiation back towards the sensor. In the case of a diffusely reflecting Lambertian surface, the backscatter value becomes independent of the incidence angle. If the surface exhibits a regular structure such as waves of a certain wavelength, it can cause positive interference of the incoming and backscattered EM radiation, the so-called Bragg scattering, which causes high backscatter values. For microwave frequencies, ripple waves on the water are of the order of the EM wavelength and

can cause high Bragg backscatter for scatterometers and SAR sensors (Section 9.3; Jackson & Apel, 2004).

Electromagnetic waves penetrating into a medium can encounter volume scattering which increases the backscattered radiation. The penetration depth again depends on the dielectric properties and porosity of the medium. In the visible EM spectrum, the penetration depth is low for sea ice and snow and much higher for water. Hence surface scattering dominates for sea ice and snow. For water, as long as it is clear and scattering bodies like sediments or frazil ice are absent, both surface and volume scattering are low and it appears dark. In the microwave spectrum, the penetration depth into seawater is of the order of millimetres at most. Melting conditions with wet snow and melt ponds mask all retrievable information of the sea ice below. For sea ice the microwave penetration depth and volume scattering are very much related to the age of the ice. Young and first-year ice have a higher salinity and are less porous than the older multi-year ice. During the ice growth and especially during the summer melt, much of the brine is removed from the ice, leaving behind fresher ice with empty brine pockets and channels (Chapter 1). These pockets and channels cause a much higher backscatter value for multi-year than for first-year ice, as can be seen in Figure 9.4(e).

So far we have discussed the influence of scattering on satellite measurements. Most of these principles are very similar for microwave emission [compare Figure 9.4c (emission) and 9.4e (backscatter)].

Many more details about scattering mechanisms, microwave emission, and sea ice remote sensing in general can be found in Ulaby et al. (1982, 1986) and Lubin and Massom (2006).

## 9.2 Microwave radiometry and scatterometry

### 9.2.1 Theory/principles of measurements

Any material emits EM radiation as a function of its physical temperature and emissivity. The emissivity  $\epsilon$  is a function of the dielectric properties of the material. Sea ice can be considered a mixture of ice crystals, brine solution and air. **The sea ice dielectric properties are mainly determined by its salinity, temperature and porosity** (Chapter 1). Snow, when dry, can be regarded

as a mixture of ice crystals and air. Wet snow has liquid water as a third component (Chapters 1 and 3).

Microwave radiation penetrates snow and sea ice. Penetration depth is closely linked to  $\epsilon$  and depends, like  $\epsilon$ , on frequency and polarization. Radiation at, for example, **89 GHz, penetrates less into sea ice than radiation at, say, 19 GHz**. EM radiation is reflected and refracted at strong dielectric property gradients such as the water–ice interface at the ice underside, the ice–air interface and the ice–snow interface. Within the ice and snow itself, the radiation is either attenuated as a function of salinity and liquid water content, or it is scattered at air inclusions, which each act as an ice–air interface. The higher the salinity and/or liquid water content in the sea ice and/or snow, the more radiation is attenuated. As a consequence, for example, the penetration depth is small and  $\epsilon$  high for thin ice and first-year ice. The larger the concentration of air inclusions, the more radiation is scattered and the lower is  $\epsilon$ , as is the case for multi-year ice. In addition to its high number of air inclusions, multi-year ice also has a low salinity, a prerequisite for enhanced scattering of microwave radiation within the ice.

Optimal for sea ice microwave remote sensing in terms of a minimum atmospheric influence are frequencies  $< 10$  GHz. Sensor antenna aperture and antenna design for a satellite sensor limit the spatial resolution at such low frequencies to several 10 km. **At higher frequencies, e.g. 89 GHz, the spatial resolution is only a few kilometres**. This is illustrated in Figure 9.4, middle row (data: <http://nsidc.org/data/amsre/>). Advanced Microwave Scanning Radiometer – **Earth (AMSR-E) brightness temperatures reveal many more details at 89 GHz (Figure 9.4c) than at 19 GHz (Figure 9.4d)** – e.g. in the Fram Strait area. Areas of elevated brightness temperatures over open water (Figure 9.4; compare 89 with 19 GHz, Barents Sea) could be misinterpreted as sea ice but are actually caused by clouds and other atmospheric influences. Therefore satellite microwave remote sensing of sea ice is a trade-off between bearable atmospheric influence and a spatial resolution that is as fine as possible.

### 9.2.2 Sea ice area

Sea ice area and extent are computed from sea ice concentration ( $C$ ): the sea ice area fraction of a known area, e.g. a grid cell. Brightness temperature ( $T_b$ ) differences between open water and sea ice are utilized to compute



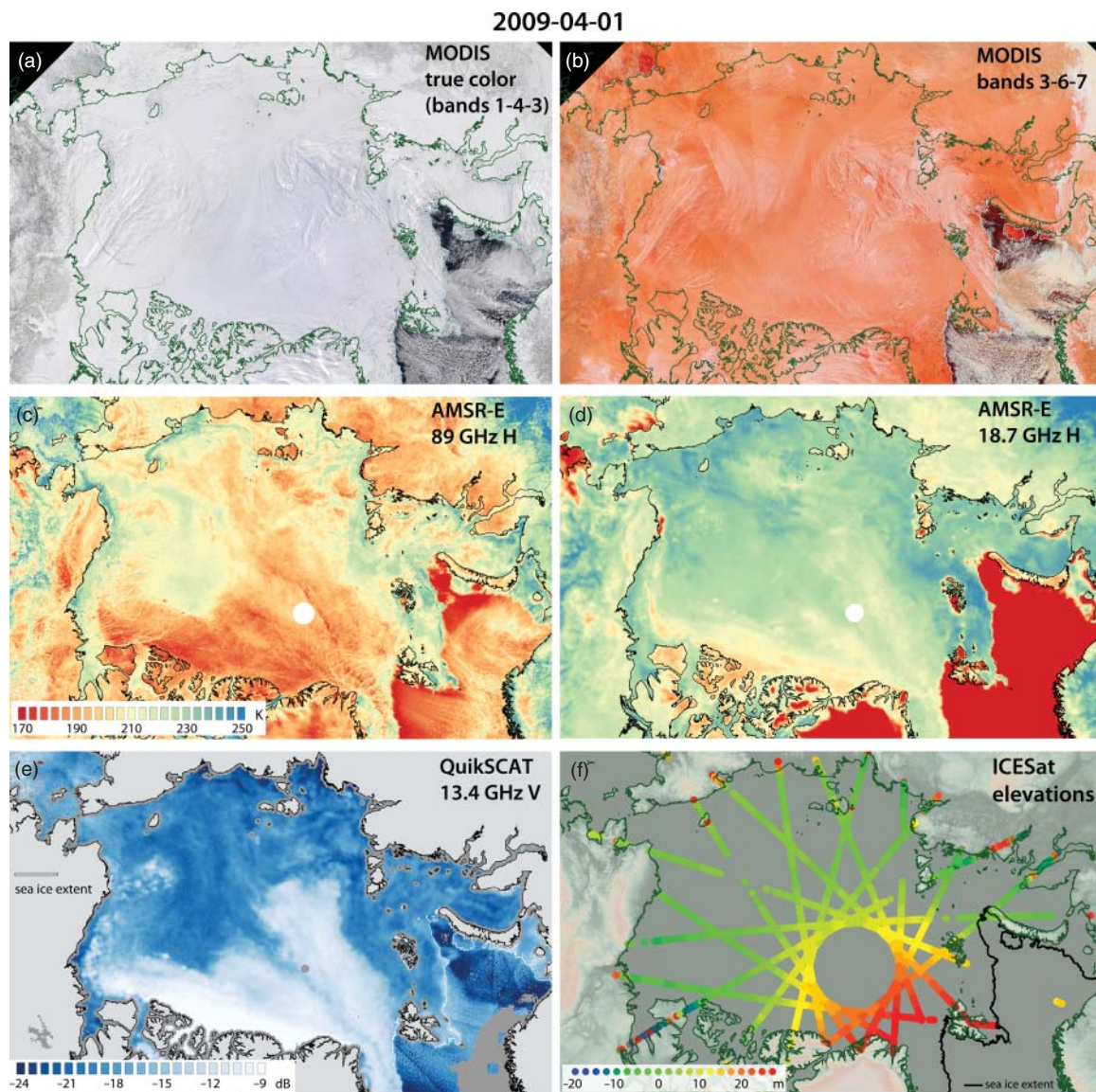


**Figure 9.4** Example of how different satellite sensors see the Arctic sea ice cover on 1 April 2009. This figure shows the ‘raw’ satellite measurements, Figures 9.6 and 9.11 show derived geophysical sea ice quantities from these measurements. (a) MODIS visible bands (645, 555, 470 nm); (b) combined MODIS blue (470 nm) and short-wavelength infrared (SWIR) bands (1.6, 2.1  $\mu\text{m}$ ); (c, d) Advanced Microwave Scanning Radiometer – Earth (AMSR-E) microwave brightness temperatures at 89 GHz H (horizontally polarized) (c) and 19 GHz H (d); (e) backscatter from the QuikSCAT scatterometer at 13 GHz ( $K_u$  band) V (vertically polarized); (f) elevations (in reference to the Earth ellipsoid) from the ICESat GLAS laser altimeter. The ICESat footprint size is about 70 m and is increased here for better visibility by factor 1000 to 70 km. The white and grey discs located at the pole in images (c)–(f) denote the area of data missing due to the satellites’ orbit inclination.

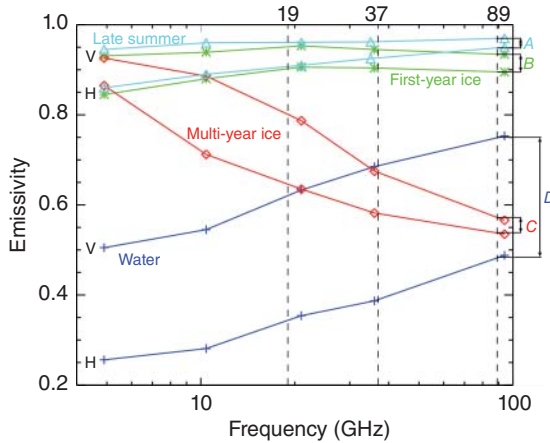


**Figure 9.5** Observations of vertically (V) and horizontally (H) polarized emissivities  $\epsilon$  of sea ice and sea water at an incident angle of  $50^\circ$  from two field campaigns. For frequencies typically used for sea ice concentration retrieval (19, 37, 89 GHz) polarization difference for water,  $D$ , is larger than for all sea ice types (A, B, C).

C. Usually the  $T_B$  of open water is smaller than the  $T_B$  of sea ice. Wind-induced roughening of the sea surface can increase open water emissivity  $\epsilon$ , and hence the  $T_B$  to the level of the sea ice  $T_B$ . Brightness temperatures measured over sea ice depend on its emissivity and physical temperature, but the  $T_B$  variability is dominated by the emissivity. Therefore  $T_B$  varies with polarization and frequency, as does  $\epsilon$ . Figure 9.5 shows surface  $\epsilon$  for different frequencies demonstrating that the polarization difference  $P = T_{BV} - T_{BH}$  (V for vertical polarization, H for horizontal) can be used to discriminate water and sea ice. To remove the dependence on the physical temperature, the polarization ratio  $PR = \frac{T_{BV} - T_{BH}}{T_{BV} + T_{BH}}$  is frequently used in sea ice algorithms.

Ivanova et al. (2014) and Andersen et al. (2006) give overviews of sea ice retrieval algorithms based on satellite microwave radiometry. Usually these algorithms combine  $T_B$  at two different polarizations (group I) or from two different frequencies (group II), or both, group III. The choice of the correct  $T_B$  combination is determined by a low sensitivity to atmospheric influence or to unwanted variations in ice and snow physical properties, a fine spatial resolution and a high accuracy.

Group I includes, for example, the COMISO Bootstrap algorithm, polarization mode (Comiso, 1986), based on 37 GHz  $T_B$  at vertical and horizontal polarization, and the ARTIST Sea Ice (ASI) algorithm (Kaleschke

et al., 2001; Spreen et al., 2008), based on the near 90 GHz polarization difference. An example of ASI AMSR-E sea ice concentration is shown in Figure 9.6(b) (data: <http://seaice.uni-bremen.de/amsr/>). Group II includes, for example, the COMISO Bootstrap algorithm, frequency mode (Comiso, 1986), based on 19 and 37 GHz  $T_B$ , vertical polarization. Group III includes, for example, the NASA-Team (NT) algorithm (Cavalieri et al., 1984) or enhanced NASA-Team (NT2) algorithm (Markus & Cavalieri, 2000), based on  $T_B$  at 19 GHz, both polarizations, and 37 GHz, vertical polarization, plus the NT2 at near 90 GHz, both polarizations. The Bristol algorithm (Smith, 1996) also belongs to this group. A fourth group comprises hybrid approaches that combine two algorithms of the above-mentioned groups. The Eumetsat OSI-SAF algorithm is one such approach, combining the COMISO bootstrap algorithm, frequency mode, with the Bristol algorithm (Eastwood et al., 2012).

Sea ice extent can be derived also from radar backscatter from scatterometers like QuikSCAT (e.g. Remund & Long, 1999). The backscatter difference between open water and sea ice allows their discrimination and mapping of the ice-covered area. Sea ice extent based on scatterometry can be more accurate than the one obtained with microwave radiometry – particularly for an ice edge dominated by frazil and grease ice (Haarpaintner et al., 2004; Rivas et al., 2012) or melting, wet ice (e.g. Ozsoy-Cicek et al., 2011).

### 9.2.3 Sea ice motion

In order to derive sea ice motion, sea ice is tracked in a pair of consecutive overlapping satellite images. This section considers sea ice motion observed with coarse-resolution [i.e. O (10 km) or coarser] satellite imagery such as microwave radiometry or scatterometry. Small-scale sea ice motion derived from fine-resolution satellite imagery is described later.

Sea ice displacement can be observed with any kind of imaging satellite sensor as long as the sensor resolves surface features, which can be tracked over time. Features can be ice floe boundaries, deformation features such as ridges, different ice types and different surface properties, as, for example, determined by the snow cover.

The most common method to track surface features in consecutive images from scatterometry or microwave  $T_B$  is the maximum cross-correlation (MCC) method. For



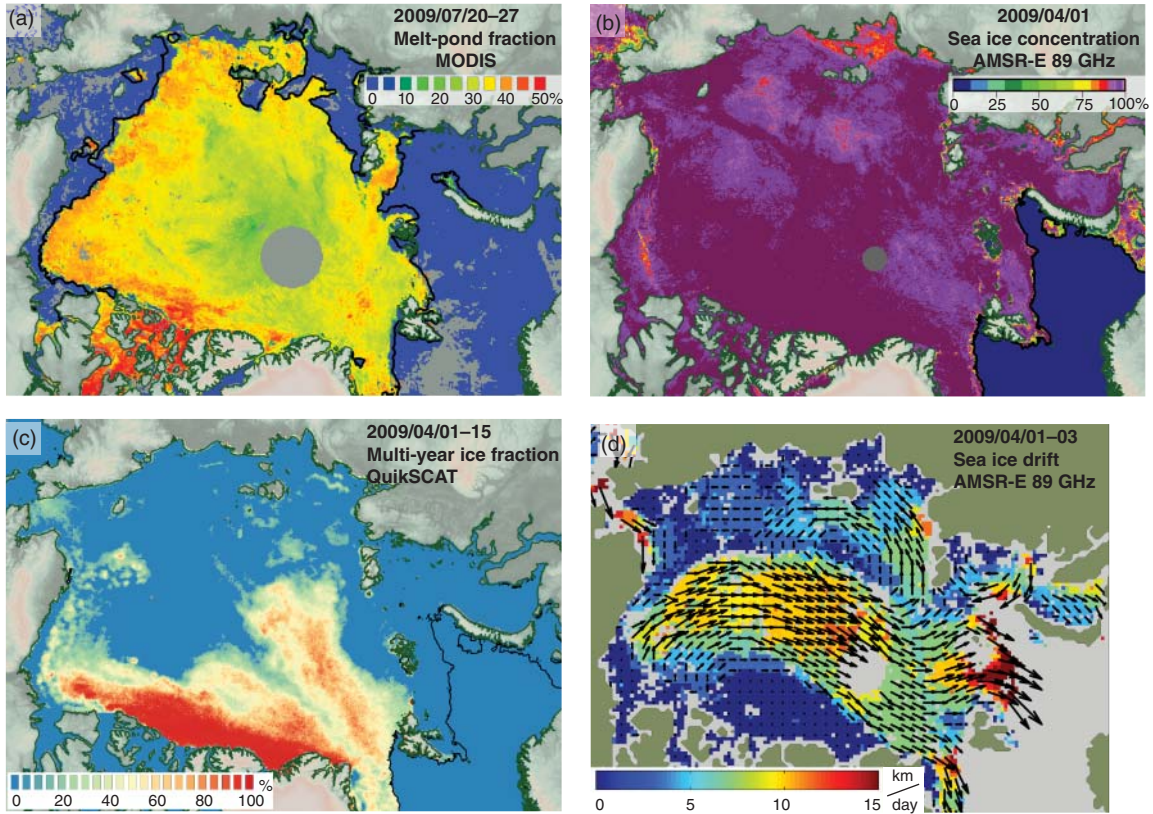


**Figure 9.6** Example of geophysical sea ice quantities derived from satellite observations (see also the correspondent raw satellite observations in Figure 9.4). (a) Melt-pond fraction from an 8-day MODIS composite for 20–27 July 2009 (grid resolution 12.5 km); (b) sea ice concentration from the Advanced Microwave Scanning Radiometer – Earth (AMSR-E) 89 GHz channels on 1 April 2009 (grid resolution 6.25 km); (c) multi-year sea ice fraction from a 15-day QuikSCAT composite for 1–15 April 2009 (grid resolution 12.5 km); (d) sea ice drift from AMSR-E 89 GHz observations between 1 and 3 April 2009 (grid resolution 31.25 km; vectors show drift direction for every third grid cell with the vector length proportional to the drift speed).

this, a box of image pixels, e.g.  $5 \times 5$ , is selected in the first satellite image. This box has a characteristic radar backscatter or  $T_B$  distribution. A new box of a similar size is moved within a certain search window around the position of the original box in the second image. For each location of the new box, the cross-correlation between the radar backscatter or  $T_B$  distribution at the current position in the second image and the original box in the first image is computed. The location providing the highest (maximum) cross-correlation gives the best match between the box in the first and second images, respectively. The distance between the centres of the two boxes is the magnitude of the displacement vector. The location of the centres relative to each other gives the direction of the displacement vector. Sea ice

drift speed is computed from the magnitude and the time difference between the two satellite image acquisitions. Typical ice drift speeds are  $5\text{--}10\text{ km day}^{-1}$ , as can be seen in the example in Figure 9.6(d) using AMSR-E 89 GHz data as input (Girard-Ardhuin & Ezraty, 2012; data: <http://cersat.ifremer.fr>).

The correlation needs to be above a certain experience-based threshold. Too low thresholds could include spurious displacement vectors; too high thresholds could discard too many vectors and hence create unwanted data gaps. The correlation threshold should depend on the season because surface features can change, e.g. by melting, as do the distributions of radar backscatter and  $T_B$  (e.g. Girard-Ardhuin & Ezraty, 2012). During melting conditions sea ice motion

retrieval is generally less reliable, if not even impossible, but alternatives exist (Kwok, 2008).

Usage of optical and infrared sensors is limited to clear-sky daylight cases. Still such imagery has been used for sea ice motion retrieval, e.g. from AVHRR imagery (Ninnis et al., 1986; Emery et al., 1991). Scatterometry (ESCAT, QuikSCAT or ASCAT) and microwave radiometry (SSM/I and AMSR-E/2) form the backbone of large-scale sea ice motion retrieval. Several sea ice drift products have been derived (e.g. Girard-Ardhuin & Ezraty, 2012; Kwok et al., 1998; Lavergne et al., 2010). Sumata et al. (2014) compare different drift products.

The grid resolution of a sea ice motion product is determined by the satellite channels used; it is of the order of 50 km or even coarser because several pixels need to be combined in a box (see earlier). This hampers retrieval of slow ice drift at daily temporal resolution. Also the sea ice motion is quantized as a function of the grid used, as shown and mitigated by Lavergne et al. (2010) introducing the continuous MCC.

### 9.2.4 Sea ice type

Radiometric and radar backscattering properties differ between different ice types as a function of their salinity, temperature, density, surface roughness and snow cover properties. Different properties can cause similar changes in  $T_B$  or radar backscatter. A good example for this is the gradient ratio ( $GR$ ) between 37 and 19 GHz  $T_B$  at vertical polarization:

$$GR_{37,19} = \frac{T_B(37V) - T_B(19V)}{T_B(37V) + T_B(19V)} \quad (9.1)$$

In the Arctic the  $GR$  is used to estimate the multi-year ice fraction, e.g. with the NT algorithm (Cavalieri et al., 1984). Thin ice and first-year ice have a  $GR$  close to zero; the  $GR$  of multi-year ice is negative. Comiso (2012) used the difference in polarization at 37 GHz to discriminate first- and multi-year ice. In the Antarctic, multi-year ice, as is typical for the Arctic, is seldom found. Melt-refreeze cycles, however, can change snow properties such that its microwave signature is similar to that of multi-year ice.

Multi-year ice or coarse-grained metamorphous snow can be identified by higher radar backscatter values (Figure 9.4e; data from: <http://cersat.ifremer.fr>) because of the larger volume scattering contribution compared with more saline and substantially less porous first-year

ice. Kwok (2004) used an empirical relationship to infer the Arctic multi-year ice fraction from QuikSCAT backscatter, as shown in Figure 9.6(c), and Lindell and Long (2016) derived and inter-compared the Arctic multi-year ice fraction derived from QuikSCAT and OSCAT-2 data.

Elevated radar backscatter is also found in the marginal ice zone, e.g. in the Barents Sea (Figure 9.4e). This could be due to a high fraction of pancake ice, which has high surface roughness and more floe edges and hence higher radar backscatter than other thin ice types or first-year ice (Dierking, 2001). Pancake ice is a likely source for the higher radar backscatter observed in the Antarctic marginal ice zone (Lange & Eicken, 1981). Alternatively, the observed elevated radar backscatter could be caused by strongly deformed ice with many ridges.

### 9.2.5 Thin sea ice thickness

The retrieval of the sea ice thickness in general is described in Section 9.4. Here we concentrate on thin ice. Approaches utilizing active microwave data (i.e. SAR; see Section 9.3) assume that the surface roughness of young and thin sea ice tends to increase with thickness and that the vertical salinity profile changes with thickness. The ratio of vertically to horizontally polarized radar backscatter (co-polarization ratio), at L- or C-band frequencies can be used empirically to infer the thickness of thin sea ice (e.g. Kwok et al., 1995; Nakamura et al., 2009). The maximum thickness to be retrieved ranges from 0.1 m (Kwok et al., 1995) to over 1 m (Nakamura et al., 2009). Most of these empirical approaches have not yet been applied widely.

Approaches utilizing microwave radiometry take advantage of the change in salinity with ice thickness. The approach using, for example, SSM/I or AMSR-E data is empirical and based on the ratio of the vertically to horizontally polarized  $T_B$  at 37 GHz (e.g. Martin et al., 2004, 2005). Even though limited to ice thickness values  $< 0.2$  m, it has been developed further and applied regionally (e.g. Nishashi et al., 2009) and hemispherically (Tamura et al., 2008; Tamura & Ohshima, 2011). A sophisticated evaluation of the results is, however, hampered by limited access to thin sea ice regions to carry out *in situ* measurements.

A physically (Kaleschke et al., 2010) and empirically (Huntemann et al., 2014) based approach utilizing the sensitivity of L band  $T_B$  to salinity and temperature

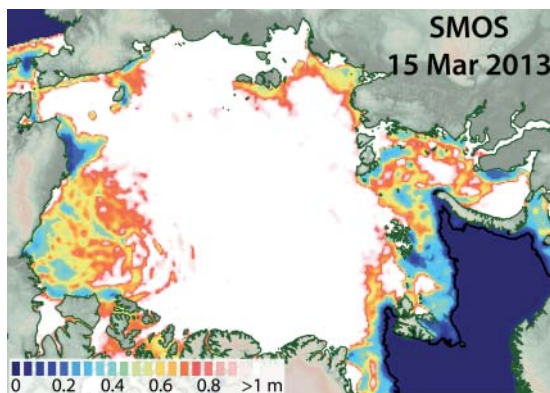


**Figure 9.7** Thin sea ice thickness derived from the Soil Moisture and Ocean Salinity (SMOS) L-band radiometer. The thickness range is limited to 0–1 m and SMOS ice thickness is most accurate below about 0.5 m. The black line shows the sea ice extent for that day.

of sea ice has been developed for measurements by the Soil Moisture and Ocean Salinity (SMOS) sensor. These approaches enable the retrieval of ice thickness up to about 0.5 m independent of daylight and weather conditions for high ice concentration under freezing conditions; for ice of low salinity, as in the Baltic Sea, the maximum thickness to be retrieved is larger (Tian-Kunze et al., 2014). An example of SMOS thin sea ice thickness for 15 March 2013 is shown in Figure 9.7 (data: [http://icdc.zmaw.de/l3c\\_sm0s\\_sit.html](http://icdc.zmaw.de/l3c_sm0s_sit.html)), which can be compared with the ice thickness from CryoSat-2 in Figure 9.11(b) (see later) for the same month (mind the different colour scales).

### 9.2.6 Snow thickness on sea ice

Snow depth  $S$  can be retrieved utilizing its empirical relationship to the gradient ratio ( $GR$ ) between  $T_B$  at 37 and 19 GHz (see equation 9.11; Markus & Cavalieri, 1998). The retrieval is limited to  $S < 50$  cm and to regions of first-year ice because the  $GR$  varies also with the multi-year ice fraction. The retrieval is influenced by grain size variations and snow wetness (Markus & Cavalieri, 1998) and underestimates snow depth for rough sea ice (e.g. Worby et al., 2008; Kern et al., 2011).

For thick sea ice, the insulating effect of a snow cover depends mainly on its depth and can be quantified by the change in ice surface temperature. Within a certain snow depth range, the increase in ice surface temperature as function of snow depth causes an increase in

the brine volume fraction, which in turn changes the microwave emissivity at L-band frequencies. Maaß et al. (2013) exploited this to derive snow depth on thick sea ice from SMOS satellite microwave radiometry at L-band frequencies under cold conditions.

### 9.2.7 Melt onset

The seasonal evolution of melt and freezing conditions can be estimated using microwave radiometry and scatterometry. In the Arctic, the moisture increase in the snow during melt causes an increase in  $T_B$  and a decrease in radar backscatter compared with values before melt. For example, Markus et al. (2009) exploited this to map melt onset on Arctic sea ice. In the Antarctic, moisture increase in the snow is less pronounced. Instead, melt–refreeze cycles are very common and change snow grain size, which has an impact on  $T_B$  variability. Willmes et al. (2009) used this to map melt onset on Antarctic sea ice.

## 9.3 Synthetic aperture radar (SAR)

### 9.3.1 Theory/principles of measurements

One of the disadvantages of the radiometer and scatterometer measurements discussed in Section 9.2 is their low spatial resolution (Tables 9.1 and 9.2). The along-track (or azimuth) resolution  $\rho_a$  of an imaging radar depends on the range distance  $R$  (i.e. distance between the satellite and the observed object; see also Figure 9.1), EM wavelength  $\lambda$ , and length of the antenna  $l$ :

$$\rho_a = \frac{R\lambda}{l}$$

To achieve a resolution of  $\rho_a = 10$  m for a C-band radar with wavelength  $\lambda = 5$  cm and a range of 800 km (typical altitude of a satellite), one would need a 4-km-long antenna, which obviously is impractical. Here the advantage of SARs comes into play. A SAR uses the along-track movement of the satellite to ‘simulate’ a long antenna. Several measurements of the small, real antenna  $A_r$  on the satellite are used to construct the measurement of a synthetic, large antenna. Every object on the Earth’s surface is covered several times by the large footprint of  $A_r$ , but under different incident angles. When an object enters the radar footprint in front of the nadir antenna position, its backscattered radar signal will be shifted to higher frequencies according

**Table 9.1** List of commonly used sensors for radiometry in sea ice research (non-exclusive).

Name	Frequency (GHz)	Resolution (km)	Swath (km)	Incidence angle	Inclination	Operational	Polarization
<b>ESMR</b>	19.4	25–150	1280	0–50°	81° retrograde	1972–1976	H
<b>SMMR</b>	6.6, 10.7, 18.0, 21.0, 37.0	30–150	780	50°	99.15°	1978–1987	H and V
<b>SSM/I; SSMIS</b>	19.4, 22.2, 37.0, 85.5 (SSMIS: 91.7 + more)	15–50	1394 (SSMIS: 1707)	53°	98.9°	1987–2009 SSMIS: 2003–	H and V 22.2 GHz: V
<b>AMSR; AMSR-E; AMSR2</b>	6.9, 10.7, 18.7, 23.8, 36.5, 89.0 (AMSR2: + more)	5–50	1450	55°	98.2°	2002–2011 AMSR2: 2012–	H and V
<b>SMOS</b>	1.4 (L band)	30–50	900	0–55°	98.44°	2009–	Full

ESMR, electrically scanning microwave radiometer; SMMR, scanning multichannel microwave radiometer; SSM/I, special sensor microwave imager; SSMIS, special sensor microwave imager/sounder; AMSR, Advanced Microwave Scanning Radiometer; SMOS, Soil Moisture and Ocean Salinity sensor; H, horizontal; V, vertical.

**Table 9.2** List of commonly used sensors for scatterometry in sea ice research (non-exclusive).

Name	Frequency (GHz)	Resolution (km)	Swath (km)	Incidence angle	Inclination	Operational	Polarization
<b>ESCAT (ERS-1 and 2)</b>	5.3 (C-band)	50	500	18–59°	98.5°	1991–2011	V
<b>QuikSCAT</b>	13.4 (K <sub>u</sub> -band)	25 × 6	1400–1800	46–54°	98.6°	1999–2009	H & V
<b>Oceansat-2</b>	13.5 (K <sub>u</sub> -band)	50	1400–1840	49–58°	98.3°	2009–2014	H & V
<b>ASCAT</b>	5.3 (C-band)	50	500 (dual swath)	25–65°	98.7°	2006–	V

to the Doppler effect. If the same object is observed again when it leaves the footprint behind the antenna, its reflected signal will be Doppler-shifted to lower frequencies. Every object is observed several times within the footprint.

If the movement of the satellite in space is known with high accuracy, the synthetic aperture of a large antenna can be constructed using the different viewing geometries. The along-track resolution,  $\rho_{SAR}$ , of a SAR is, perhaps surprisingly, proportional to the real antenna length,  $l$  – i.e. the shorter the antenna, the higher the SAR resolution:

$$\rho_{SAR} = \frac{l}{2}$$

The resolution  $\rho_{SAR}$  is independent of wavelength  $\lambda$  and range distance  $R$ . The returned power, however, still depends on the emitted signal strength, which in turn also depends on the antenna size. To achieve a suitable signal-to-noise ratio, there is a lower limit to how small a SAR antenna can be. Typical SAR antenna lengths are between 5 and 15 m, offering a SAR resolution down to  $\rho_{SAR} = 2$  m.

As for traditional radars, the across-track (slant range) resolution  $\rho_r$  depends on the pulse length  $\tau$  of the SAR and the incidence angle  $\theta$ :

$$\rho_r = \frac{c\tau}{2 \sin \theta}$$

where  $c$  is the speed of light. As for  $\rho_{SAR}$ ,  $\rho_r$  is also independent of the  $\lambda$  and  $R$ . The radar bandwidth  $B$ , however, and therefore the pulse width  $\tau = 1/B$  depend on  $\lambda$ .

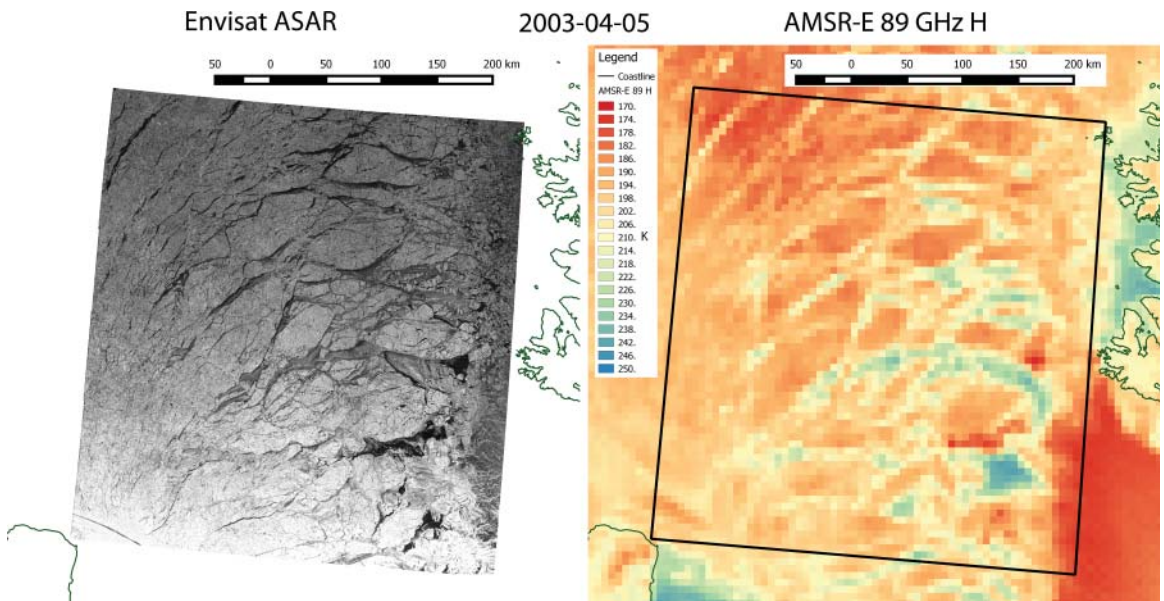
These are only a few of the basic principles of SAR remote sensing. A more complete description can be found in Jackson and Apel (2004). An overview of the most commonly used SAR sensors for sea ice research is given in Table 9.3.

Figure 9.8 shows an example of the much higher resolution of an Envisat ASAR ScanSAR wide swath mode scene in comparison to AMSR-E radiometer observations at 89 GHz. The high resolution of 50–150 m for scenes of about 400–500 km in ScanSAR wide swath mode makes SAR data well suited for operational application. For national ice services (e.g. NIC USA, CIS



**Table 9.3** List of commonly used synthetic aperture radar (SAR) sensors in sea ice research (non-exclusive).

Name	Frequency (GHz)	Resolution (m)	Swath (km)	Incidence angle	Inclination	Operational	Polarization
ERS-1 and 2	5.3 (C-band)	30	100	20–26°	98.5°	1991–2011	VV
Envisat ASAR	5.3 (C-band)	30–1000	100–400	15–45°	98.5°	2002–2012	Dual-polarimetric
Radarsat-1 & 2	5.3/5.4 (C-band)	3–100	18–500	10–60°	98.6°	1995–	HH (RS-1) full (RS-2)
Sentinel-1	5.4 (C-band)	5–100	80–400	19–47°	98.2°	2014–	Full
TerraSAR-X	9.6 (X-band)	1–40	5–200	15–60°	97.4°	2007–	Full
ALOS-1 & 2 PALSAR	1.3 (L-band)	3–100	20–350	8–70°	98.7° (AL-1) 97.9° (AL-2)	2006–2011 2014– (AL-2)	Full
COSMO-SkyMed	9.6 (X-band)	1–100	10–100	16–51°	97.9°	2007– Four satellites	Dual-polarimetric



**Figure 9.8** Comparison of a synthetic aperture radar (SAR) image with 150 m spatial resolution (but limited coverage) with the Advanced Microwave Scanning Radiometer – Earth (AMSR-E) radiometer observations at 89 GHz and about 5 km resolution on 5 April 2003. Similar features in the ice can be observed but with much different detail.

Canada, MET Norway, DMI Denmark), SAR data are the key information for deriving ice charts for their area of interest. Onstott & Shuchman (2004) and Dierking (2013) give a more extensive overview of SAR sea ice remote sensing.

**9.3.2 Sea ice motion**

If a consecutive series of SAR images is available for a given region, sea ice motion can be derived in a similar fashion to that described in Section 9.2.3 (e.g.

Kwok et al., 1990; Komarov & Barber, 2014), but with a much higher spatial resolution. The SAR scene is divided in sub-regions. These are identified again in a subsequent scene using a cross-correlation method (MCC; see Section 9.2.3). The quality of the results depends on the time difference between the two SAR scenes, which should be as short as possible. The original cross-correlation method can be improved by several additions: a hierarchical approach where ice motion is first calculated with lower resolution patterns as a first

guess before resolution is improved in several steps in a pyramid-like way. Correlations cannot only be calculated between patterns of the backscatter magnitudes in the space domain but also using a Fourier transform in the frequency domain (Komarov & Barber, 2014). If a pattern match is found its quality can be assessed calculating the back-trajectory from the second to the first scene.

The sea ice motion derived from SAR can have spatial resolutions finer than 10 km and, more importantly, uncertainties of the displacement vector are on the order of a few hundred metres (e.g. Hollands & Dierking, 2011). SAR sea ice motion is therefore well suited to observing small scale sea ice kinematic features caused by ice deformation. The Radarsat Geophysical Processor System (RGPS) (e.g. Kwok et al., 1990; Kwok, 2006) follows a grid of sea ice parcels over a complete season in a Lagrangian way. The initial grid distance is 10 km. The grid cells get deformed over time. Figure 9.9 shows the RGPS sea ice divergence, shear and vorticity for November 1999 (data: <http://rkwok.jpl.nasa.gov/radarsat>). Clearly linear kinematic features spanning several hundreds of kilometres over the Arctic Basin can be identified. Due to its high resolution and accuracy, SAR sea ice motion is ideally suited for such sea ice deformation, i.e. strain rate observations.

In the marginal ice zone where rotation of floes becomes more prevalent and the ice gets broken up, feature and object tracking approaches are commonly used and better suited than the cross-correlation method (e.g. Kwok et al., 1990).

### 9.3.3 Sea ice type

Sea ice types can be discriminated in SAR data in a similar manner to microwave radiometers and scatterometers (Section 9.2.4): multi-year ice shows a higher volume scattering than first-year ice (Section 9.1.4); deformed ice with ridges shows higher radar backscatter than level ice; and rough surfaces, e.g. pancake ice or frost flowers, or an increased number of floe edges for broken up ice increase the radar backscatter, etc. The much higher spatial resolution of SAR data, however, allows a much more detailed classification and a larger number of different surface types to be identified: in Figure 9.8 single floes and open and refrozen leads can be clearly identified in the ASAR data compared to the AMSR-E data. The high-resolution SAR modes (Table 9.3) allow identification of melt ponds or ridges. In single polarization SAR images, many ambiguities can exist between ice types and even wind roughened water and ice. Still ice type segmentation can be successfully applied and can even be used in an operational context (Ochilov & Clausi, 2012). The dual- and full-polarimetric modes of today's SAR sensors allow an even better segmentation of surface types (e.g. Moen et al., 2013), e.g. for ice versus water separation or identifying multi-year ice floes embedded in first-year ice. Different SAR frequencies have different strengths: deformed ice can be better discriminated at L-band than at C- and X-band frequencies, while the higher frequencies are better for multi-year versus first-year ice discrimination (e.g. Dierking, 2013).

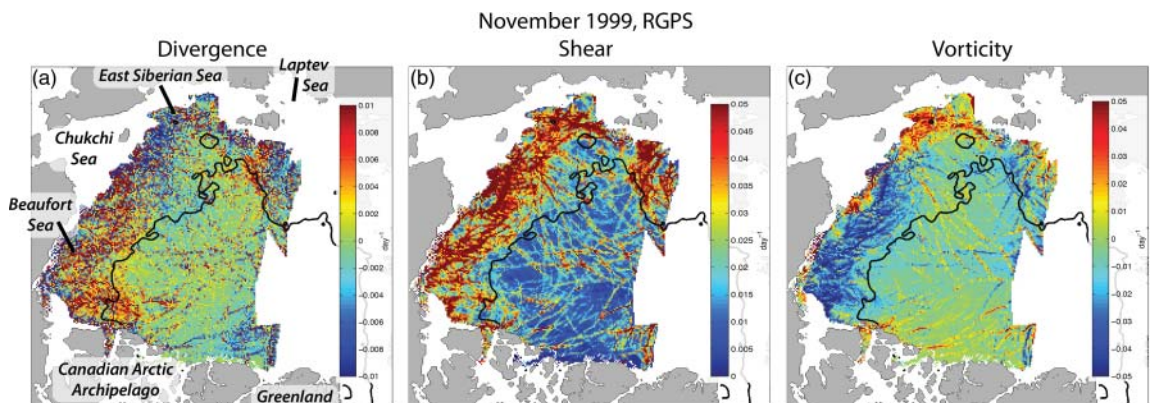


**Figure 9.9** Sea ice strain rates calculated from sea ice motion using Radarsat-1 synthetic aperture radar (SAR) data for November 1999: (a) divergence; (b) shear; and (c) vorticity. The black line shows the multi-year sea ice extent from QuikSCAT data.



## 9.4 Altimetry

### 9.4.1 Theory/principles of measurements

Both spaceborne laser and radar altimeters can be used to retrieve the sea ice thickness  $I$ . The sea ice thickness is not measured directly but is inferred from the sea ice freeboard  $F$ , the part of the sea ice sticking out of the ocean. Radar altimeter data of sea ice have been available since the launch of ERS-1 in 1991 with the pulse-limited radar altimeter on board, covering the sea ice up to  $82^\circ$  latitude. ERS-1 was followed by ERS-2 and Envisat in similar orbits. The first spaceborne laser altimeter and the first altimeter covering the Arctic sea ice up to  $86^\circ\text{N}$  was the GLAS instrument on ICESat, operational from 2003 to 2009. The first radar altimeter using synthetic aperture processing and covering the area up to  $88^\circ\text{N}$  was CryoSat-2 launched in 2010.

Both laser and radar altimeters send out an EM pulse in nadir direction that is reflected back to the satellite by the Earth's surface. The amplitude of the returned power of the pulse is recorded within a short receiving time window. These digitized pulses are referred to as laser or radar waveforms and have a Gaussian, peaky shape for flat surfaces, such as leads, and a wider shape with a long tail for rough, scattering surfaces, such as sea ice. The location  $T_r$  of the first return signal related to the surface at nadir position, i.e. closest to the satellite, is now re-tracked from the waveform. Different waveform re-trackers for different surfaces and application exist (e.g. Zwally et al., 2002; Kurtz et al., 2014; Ricker et al., 2014). Typically, the waveform is re-tracked on the

leading edge for sea ice surfaces and on the maximum peak for the smooth, Gaussian ocean or thin sea ice surfaces in leads (Laxon et al., 2013). From the travelling time  $\Delta t$  for the identified return point  $T_r$  and the speed of light  $c$  the distance  $D = c \Delta t / 2$  between the altimeter and the Earth's surface is calculated (see Figure 9.10). To get from the measured distance  $D$  to a surface elevation measurement  $E$ , the exact position of the altimeter, and thus the position of the satellite in space, has to be known with centimetre accuracy. The position of the satellite,  $h_{\text{ellip}}$ , is measured in reference to an Earth ellipsoid model. The surface elevation  $E$  is calculated as  $E = h_{\text{ellip}} - D$  (an example for ICESat is shown in Figure 9.4f).

The shape of the recorded laser and radar waveforms also contains information about surface roughness and type (e.g. Zygmuntowska et al., 2013). The most important application of altimetry in sea ice research, however, is the retrieval of sea ice freeboard and thickness as, will be discussed in the next subsection.

### 9.4.2 Sea ice thickness

A prerequisite to obtaining the sea ice thickness  $I$  from altimeter measurements is the sea ice freeboard height  $F$  (an example for laser altimeters is shown in Figure 9.10). A major challenge in determining the freeboard  $F$  from altimetry is the identification of leads in between the ice floes. Leads with open water or covered by thin sea ice serve as reference points for the sea surface height (SSH). The difference between the SSH and the elevations  $E$  measured over the sea ice is the wanted

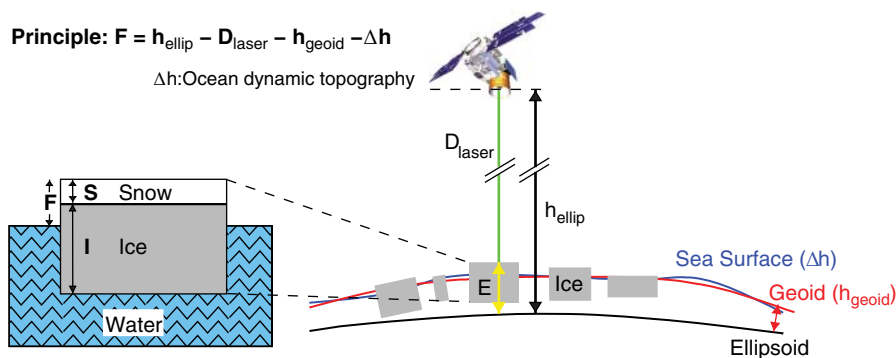


**Figure 9.10** Schematic showing the principles of sea ice freeboard and thickness retrieval from satellite altimetry using the ICESat laser altimeter as an example. Left side: interrelation of sea ice freeboard,  $F$ , snow depth,  $S$ , and sea ice thickness,  $I$ . Right side: an artist's view of ICESat above the three involved surfaces: reference ellipsoid (black), geoid (red), and sea surface (blue). Figures are not to scale.

freeboard  $F$ :

$$F = E - h_{\text{geoid}} - \text{SSH}$$

where  $h_{\text{geoid}}$  is the Earth geoid height. The SSH varies in respect to the geoid according to the tides, ocean currents and atmospheric pressure. The SSH is not known with a high enough accuracy from other sources but has to be determined from the altimeter measurements themselves. Leads and thereby the SSH can be identified by the shape of the laser waveforms or the comparable lower elevation of the leads compared with the surrounding sea ice. The development of methods to determine the SSH in sea ice-covered regions is still an active field of research. One challenge for the SSH determination is the large footprint size, especially of radar altimeters. While ICESat's laser footprint has a diameter of about 70 m, CryoSat-2's radar footprint is  $380\text{ m} \times 1650\text{ m}$ , and the footprint of all former radar altimeters is several km large (Table 9.4). In most cases leads are much smaller than that and have to be detected at sub-footprint size for accurate SSH retrieval. The specular reflection caused by leads, however, can be identified in the retrieved radar waveform even if the lead only covers a fraction of the footprint.

The freeboard heights can be converted to ice thickness under the assumption of isostatic balance of the ice floes in the water and knowledge of all involved densities  $\rho_x$  and snow depth  $S$ . According to Archimedes' principle, a body submerged in a liquid such as water will displace the volume of water equivalent to its own weight. If now the part of the body, in our case sea ice (with snow), sticking out of the water (the freeboard) is known, the mean sea ice thickness of the floe can be determined.

The signal of a laser altimeter such as the one on board ICESat is reflected at the snow surface on top of the sea

ice. This example is shown in Figure 9.10 and the conversion between the snow freeboard,  $F_S$ , and ice thickness,  $I$ , can be described as:

$$I = F_S \frac{\rho_W}{\rho_W - \rho_I} + S \frac{\rho_S - \rho_W}{\rho_W - \rho_I} \quad (\text{for laser altimeter}) \quad (9.2)$$

Radar signals penetrate the snow either completely or partially. The signal of a radar altimeter therefore originates from either the sea ice surface or from somewhere in the snow pack. The exact origin of the radar altimeter return signal is often unknown (e.g. Willatt et al., 2010; Ricker et al., 2015). We will refer to the freeboard height measured by a radar altimeter as radar freeboard  $F_R$  that can be converted to ice thickness  $I$  by:

$$I = F_R \frac{\rho_W}{\rho_W - \rho_I} + S \frac{\rho_S}{\rho_W - \rho_I} \quad (\text{for radar altimeter}) \quad (9.3)$$

where  $S$  is the snow thickness above the radar return origin. From equations (9.2) and (9.3) it becomes obvious that accurate knowledge of snow depth  $S$  and the three densities  $\rho_x$  is needed and that the uncertainty of these variables will have a direct feedback on the accuracy of the retrieved ice thickness. Besides the uncertainty of the freeboard retrieval itself uncertainties in snow depth and ice density were identified as the most significant sources for the accuracy of the derived sea ice thickness (e.g. Giles et al., 2007; Kwok & Cunningham 2008; Kern & Spreen 2015; Ricker et al., 2015). For representative density estimates extended and repeated field in-situ measurements are of utmost importance. The same holds for a snow depth climatology. Snow depth, however, can also be estimated from airborne snow radar campaigns (e.g. Operation Ice-Bridge; Kurtz et al., 2013) or satellite radiometers (see Section 9.2.6) but often with significant uncertainties or limited spatial coverage.

**Table 9.4** List of radar and laser altimeters used for sea ice thickness retrieval.

Name	Frequency	Footprint	Inclination	Operational
<b>ERS 1 and 2 radar altimeters</b>	13.8 GHz ( $K_u$ -band)	16–20 km	98.5°	1991–2011
<b>Envisat RA-2</b>	13.575 GHz ( $K_u$ -band)	2–10 km	98.5°	2002–2012
<b>CryoSat-2</b>	13.575 GHz ( $K_u$ -band)	1650 m x 380 m	92°	2010–
<b>SARAL/AltiKa</b>	35.75 GHz ( $K_a$ -band)	8 km	98.5°	2013–
<b>Sentinel-3 SRAL</b>	13.575 ( $K_u$ -band)	2 km x 300 m	98.65°	2016–
<b>ICESat</b>	1064 nm (laser)	64 m	94°	2003–2009
<b>ICESat-2</b>	532 (laser)	10 m; 3 pairs of beams 3 km apart	94°	Launch 2017

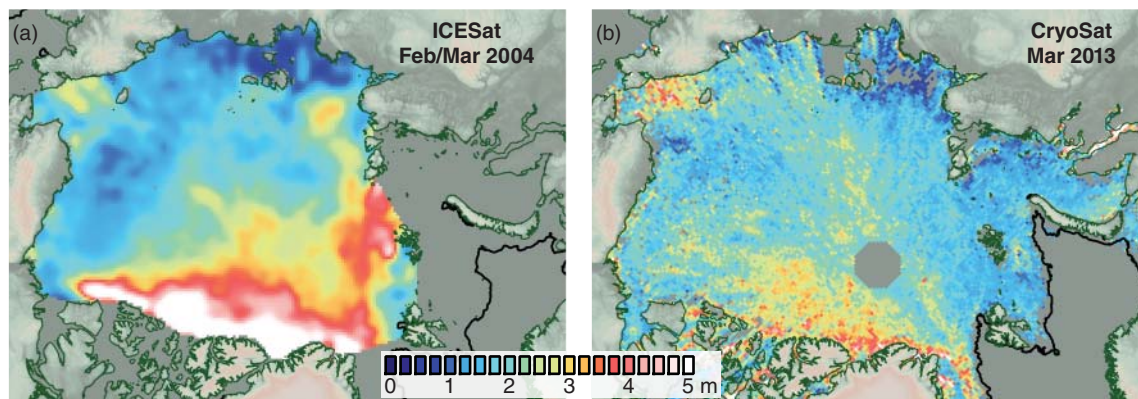


**Figure 9.11** Sea ice thickness derived from satellite altimetry. (a) For February/March 2004 from the ICESat GLAS laser altimeter; (b) 9 years later for March 2013 from the CryoSat SIRAL radar altimeter. Both datasets are shown on a 25 km grid. The ICESat data are restricted to the Arctic Basin and interpolated for empty grid cells such as the pole hole. Black lines show sea ice extent for 1 March 2004 and 15 March 2013, respectively.

Figure 9.11 shows the monthly Arctic sea ice thickness for February/March 2004 from the ICESat laser altimeter (Kwok et al., 2009; data: <http://rkwok.jpl.nasa.gov/icesat/>) and for March 2013 from CryoSat-2 radar altimeter measurements (Ricker et al., 2014; data: Hendricks et al., 2013). The Arctic ice thickness decreased between these years (Laxon et al., 2013) but shows high interannual variation (Tilling et al., 2015). ICESat and CryoSat-2 observations can now be combined to retrieve a longer-term ice thickness record (Kwok & Cunningham, 2015).

The development of new sea ice thickness retrieval methods from satellite altimeters is ongoing. Improved sea ice thickness estimates can be expected from new methods, better validation, and new sensors such as those on ICESat-2 in the future.

## 9.5 Optical and thermal infrared imaging

### 9.5.1 Theory/principles of measurements

Sea ice reflects solar radiation to a much greater extent than open water – provided there is a large enough solar elevation angle. Hence sea ice has an average albedo  $> 0.6$ , whereas water has a low albedo, 0.07. The albedo usually increases with ice thickness for bare ice (Wadhams, 2000; Brandt et al., 2005). Snow on sea ice increases the albedo substantially, usually to  $> 0.8$  (Brandt et al., 2005). Figure 9.4(a,b) show examples of MODIS visible and short-wavelength infrared (SWIR)

channel composites (data: <http://lance-modis.eosdis.nasa.gov>). Satellite sensors measuring the surface reflectance in the optical frequency range of the EM spectrum can be used to obtain the surface albedo. Estimation of the melt-pond fraction (Rösel et al., 2012) and detection of polynyas and leads are typical applications of satellite optical remote sensing of sea ice. Optical satellite imagery proved valuable for the evaluation of sea ice concentration (e.g. Comiso & Steffen, 2001). An overview of commonly used sensors is given in Table 9.5.

Sea ice emits thermal radiation according to its infrared emissivity and surface temperature,  $T_{\text{Surface}}$ . Sensors measuring  $T_{\text{Surface}}$  operate in the atmospheric window at wavelengths of 8–12  $\mu\text{m}$  (Figure 9.2). At these wavelengths, the infrared emissivity of sea ice and snow is relatively constant around 0.98 (e.g. Rees & James, 1992). Typical application areas for satellite infrared imagery of sea ice are  $T_{\text{Surface}}$  retrieval (Key and Haefliger, 1992; Hall et al., 2004), lead and polynya detection (e.g. Willmes & Heinemann, 2015, 2016) and thin ice thickness retrieval (Section 9.5.2).

Despite a requirement for daylight and clear-sky conditions, optical and infrared satellite imagery has also been used to derive sea ice concentration (Emery et al., 1994; Drüe & Heinemann 2004), and sea ice motion (e.g. Emery et al., 1991).

In the optical spectrum, the reflectivity of clouds is similar to the one of ice. Also, over ice the physical and thus infrared temperatures of clouds and the surface are similar for infrared data. Hence, even though sensors such as MODIS are equipped with numerous channels at

**Table 9.5** List of commonly used optical and thermal infrared satellite sensors in sea ice research (non exclusive). If a parameter changed between earlier and current versions of the sensors both are given.

Name	Frequency range	Number of bands	Spatial resolution	Swath	Inclination	Operational
AVHRR	630 nm–12 $\mu$ m	4–6	1090 m	2900 km	98°–99°	1978–
MODIS	405 nm–14.4 $\mu$ m	36	250–1000 m	2330 km	98.2°	1999–
MERIS	390–1040 nm	15	300–1200 m	1150 km	98.4°	2002–2012
Landsat	480 nm–11.5 $\mu$ m	7–8	80 m to 15–60 m	185 km	98°–99°	1972–
OLCI	400–1020 nm	21	300–1200 m	1270 km	98.65°	2016–

different wavelengths, cloud detection is still not optimal (e.g. Chan & Comiso, 2013). As shown in Figure 9.4(b), detection of some clouds over ice is possible with MODIS. Ice reflects in the blue channel 3 and absorbs in the SWIR infrared channels 6 and 7. Cloud droplets and crystals scatter in all three channels, which let them appear bright. The ocean absorbs in all three channels.

### 9.5.2 Thin sea ice thickness

The ice  $T_{\text{Surface}}$  can be used to estimate the thickness  $h$  of thin sea ice. It is assumed that the heat flux through sea ice is balanced by the net surface heat flux  $F_{\text{net}}$ , comprising the turbulent latent  $F_L$  and sensible heat flux  $F_S$ , and the long- and short-wave radiative fluxes,  $F_{\text{Long}}$  and  $F_{\text{Short}}$ , at the ice surface. The upward  $F_{\text{Long}}$  can be computed from the ice  $T_{\text{Surface}}$ . The downward  $F_{\text{Long}}$  can be taken from numerical weather prediction models. During winter,  $F_{\text{Short}}$  can be neglected. Turbulent heat fluxes are usually computed via bulk formulas relating near surface vertical temperature ( $F_S$ ) and moisture ( $F_L$ ) gradients to wind speed and transfer coefficients of heat and moisture (e.g. Yu & Lindsay 2003; Ohshima et al., 2009). The heat flux through the sea ice is assumed to be linearly proportional to the temperature difference between the ice surface  $T_{\text{Surface}}$  and the ice underside  $T_0$ . The proportionality coefficient is the conductive heat flux coefficient  $k$ . It is a function of sea ice salinity, temperature and thickness. This assumption holds for bare growing sea ice < 30–50 cm thick (Yu & Rothrock 1996; Drucker et al., 2003):

$$h = \frac{k(T_{\text{surface}} - T_0)}{F_{\text{net}}}$$

Snow on the thin ice disturbs the linearity assumption. Computation of the above-mentioned fluxes can be subject to large uncertainties. Observations of near-surface air temperature, humidity and wind speed

are sparse in polar regions. Models or reanalyses often do not resolve the larger heat flux through thin ice (Willmes et al., 2011). For Antarctic coastal polynyas, models or reanalyses often fail to capture the influence of the Antarctic topography (Petrelli et al., 2008). The alternative to using model data is taking *in situ* observations at, for example, automatic weather stations (e.g. van Woert, 1999).

### 9.5.3 Melt-pond fraction

Surface properties of sea ice can be extremely variable – partly due to the snow cover and its interaction with the sea ice. A few of them were considered earlier, but there are others, such as grain size, wetness, melt-pond coverage and snow morphology. Here the focus is on melt ponds and the seasonal melt–refreeze cycle.

Melt ponds occur on Arctic sea ice as a result of snow and ice surface melt every summer. They can cover up to between 50% and 60% (90% in extreme cases) of the sea ice area (Fetterer & Untersteiner, 1998). Melt ponds can cause substantial biases in the summertime sea ice concentration computed from satellite microwave radiometry (Comiso & Kwok, 1996).

Melt ponds are typically smaller than 10 m<sup>2</sup> (Perovich et al., 2002). They cannot be detected by current satellite sensors pond by pond. More common are approaches estimating the contribution of the melt-pond fraction to the measured EM signal. Landsat, MODIS and MERIS have been used to identify melt ponds and to retrieve their aerial fraction (Markus et al., 2003; Tschudi et al., 2008; Istomina et al., 2015). Melt-pond cover fraction can be obtained, e.g. from 8-day composite clear-sky MODIS optical imagery using a spectral unmixing approach (Rösel et al., 2012; see the example in Figure 9.6a; data: <http://icdc.cen.uni-hamburg.de>). Reflectances from MODIS bands 1, 2

and 3 are combined utilizing the fact that reflectances of the surface types – melting snow or bare ice, and melt ponds – depend on the wavelength whereas the reflectance of open water between ice floes does not. By assuming that the reflectance measured at each band is composed of contributions from these surface types, the aerial fraction of the surface types is estimated. Rösel et al. (2012) used the approach to obtain Arctic-wide melt-pond cover fraction with an accuracy of about 5–10%.

## 9.6 Uncertainties and validation

This chapter has given an overview of the different methods used to derive sea ice quantities from satellite observations. All these methods contain several uncertainties, which will determine the quality of the final products. The estimation of uncertainties is an integral part of remote sensing of sea ice. Uncertainty ranges should always be published together with the satellite observations to allow sensible use of the products. In many cases, the estimation of the uncertainty is more challenging than the retrieval of the sea ice quantity itself. This section can only briefly summarize the different uncertainty sources and validation strategies for satellite data.

### 9.6.1 Sources of uncertainties

The first source of uncertainty is the accuracy of the measurement of the satellite sensor itself. Repeated measurements of the same target will give slightly different results caused by, for example, the sensor noise. This defines the precision of the measurement. In addition, a measurement system can have an offset or bias. Bias and precision together define the accuracy of the measurement. Constant biases are often uncritical as they can be easily corrected for. Some biases, however, change over time, e.g. those caused by degradation of a satellite sensor. This can introduce artificial trends in satellite time series, which are sometimes hard to discriminate from natural trends in the observed variable.

The satellite, in most cases, does not measure the wanted geophysical sea ice variable directly (see Sections 9.2–9.5): microwave brightness temperatures have to be converted to sea ice concentration, altimeter elevations have to be converted to ice freeboard and

thickness, etc. This conversion, also called model, includes many error sources from which we list a few here:

- The algorithm used to map measurements to geophysical quantities contains errors or there simply is no direct analytical relationship between the two and the algorithm can only produce an approximation.
- The environmental conditions, e.g. the atmosphere, influence the measurement. The influence varies for different frequencies (e.g. clouds and haze in the optical and water vapour and ocean wind roughening in the microwave spectrum). In most cases, these environmental conditions are not well enough known and cause significant uncertainties.
- Variability within the satellite footprint. Satellite measurements integrate over the footprint area, which in many cases is several kilometres (see Tables 9.1–9.4). Within the footprint, different surface types of unknown distribution can exist. Assumptions are made, as for sea ice concentration, that the footprint is composed of the two distinct surface types, water and sea ice. In reality, the surface is much more complex (different ice types, calm and wind roughened water, etc.), which will cause uncertainty in the retrieval.

The combination of measurement accuracy and all other unknowns and errors determines the uncertainty of the derived sea ice variable. Some of these factors can be theoretically determined, but many cannot. In the end, however, validation experiments are needed to quantify the uncertainties of the satellite dataset.

### 9.6.2 Validation

*In situ* measurements are used to evaluate and validate satellite products. As the polar regions are sparsely populated and challenging to reach, *in situ* data in general are sparse. Dedicated validation campaigns by ships, helicopter and airplanes are conducted to collect satellite validation datasets. In many cases, detailed knowledge of the sea ice characteristics, as for example the ice stratigraphy or snow structure, is needed to more correctly interpret the satellite measurements and to quantify the uncertainties. On the other hand, the large spatial scales of satellite measurements demand a large number of measurements over larger distances. Therefore, a dual strategy is often used for satellite product validation: detailed measurements on the ice, typically done as ice stations from ships, deliver the required detail, and airborne observations from



helicopters or airplanes bridge the gap between the small-scale ice station and often large-scale satellite measurements. One of the challenges is to estimate how many validation measurements within a satellite footprint are needed to represent the satellite measurement. The same is the case for the large-scale distribution (estimation of the covariance). It has to be estimated how many satellite measurements, i.e. footprints, have to be validated to make a sensible statement of the satellite product uncertainty on a hemispheric scale. The already-mentioned possible drift in time of satellite sensors further complicates the situation and demands repeated validation measurements throughout the lifetime of a satellite or a family of satellite sensors operated in parallel, such as SSM/I and SSMIS.

## 9.7 Acknowledgements

We gratefully acknowledge the provision of satellite datasets to produce the figures: MODIS, ICESat, QuikSCAT and RGPS data by NASA; Envisat ASAR, CryoSat-2 and SMOS data by ESA; AMSR-E data by JAXA and NSIDC; QuikSCAT data and sea ice motion by CERSAT/IFREMER; melt pond-fraction and SMOS ice thickness by ICDC/University of Hamburg; CryoSat-2 ice thickness by AWI; sea ice concentration by the University of Bremen. Parts of Figure 9.2 are courtesy of NASA.

## References

- Andersen, S., Tonboe, R., Kern, S. & Schyberg, H. (2006) Improved retrieval of sea ice total concentration from spaceborne passive microwave observations using numerical weather prediction model fields: An intercomparison of nine algorithms. *Remote Sensing of Environment*, **104**, 374–392.
- Brandt, R.E., Warren, S.G., Worby, A.P. & Grenfell, T.C. (2005) Surface Albedo of the Antarctic sea ice zone. *Journal of Climate*, **18**, 3606–3622.
- Campbell, J.B. & Wynne, R.H. (2011) *Introduction to Remote Sensing*, 5th edn. Guilford Press.
- Cavalieri, D.J., Gloersen, P. & Campbell, W.J. (1984) Determination of sea ice parameters with the NIMBUS-7 SMMR. *Journal of Geophysical Research*, **89**, 5355–5369.
- Chan, M.A. & Comiso, J.C. (2013) Arctic cloud characteristics as derived from MODIS, CALIPSO, and CloudSat. *Journal of Climate*, **26**, 3285–3306.
- Comiso, J. C. (1986) Characteristics of Arctic winter sea ice from satellite multispectral microwave observations. *Journal of Geophysical Research*, **91**, 975–995.
- Comiso, J.C. (2012) Large Decadal Decline of the Arctic Multi-year Ice Cover. *Journal of Climate*, **25**, 1176–1193.
- Comiso, J.C. & Kwok, R. (1996) Surface and radiative characteristics of the summer Arctic sea ice cover from multisensor satellite observations. *Journal of Geophysical Research*, **101**, 28 397–28 416.
- Comiso, J.C. & Steffen, K. (2001) Studies of Antarctic sea ice concentrations from satellite data and their applications. *Journal of Geophysical Research*, **106**, 31361–31385.
- Dierking, W. (2001) Radar signatures of pancake and frazil ice – a review. CONVECTION Report No. 7, v01, October 2001, EU-Final Report for Contract EVK2-2000-0058.
- Dierking, W. (2013) Sea ice monitoring by synthetic aperture radar. *Oceanography*, **26**, 100–111.
- Drucker, R., Martin, S. & Moritz, R. (2003) Observations of ice thickness and frazil ice in the St. Lawrence Island polynya from satellite imagery, upward looking sonar, and salinity/temperature moorings. *Journal of Geophysical Research*, **108**, 3149.
- Drüe, C. & Heinemann, G. (2004) High-resolution maps of the sea-ice concentration from MODIS satellite data. *Geophysical Research Letters*, **31**, L20403.
- Eastwood, S., Larsen, K.R., Laverne, T., Nielsen, E. & Tonboe, R. (2011) EUMETSAT OSI SAF Global Reprocessed Sea Ice Concentration dataset v1.1, Product User Manual v1.3. October 2011, SAF/OSI/CDOP/met.no/TEC/MA/138.
- Emery, W.J., Fowler, C.W. & Maslanik, J. (1994) Arctic sea ice concentration from special sensor microwave imager and advanced very high resolution radiometer satellite data. *Journal of Geophysical Research*, **99**, 18 329–18 342.
- Emery, W.J., Fowler, C.W., Hawkins, J. & Preller, R.H. (1991) Fram Strait satellite image-derived ice motions. *Journal of Geophysical Research*, **96**, 4751–4768.
- Fetterer, F. & Untersteiner, N. (1998) Observations of melt ponds on Arctic sea ice. *Journal of Geophysical Research*, **103**(C11), 24821–24835.
- Giles, K., Laxon, S., Wingham, D. et al. (2007) Combined airborne laser and radar altimeter measurements over the Fram Strait in May 2002. *Remote Sensing of Environment*, **111**, 182–194.
- Girard-Ardhuin, F. & Ezraty, R. (2012) Enhanced Arctic sea ice drift estimation merging radiometer and scatterometer data. *IEEE Transactions Geoscience and Remote Sensing*, **50**, 2639–2648.
- Haarpaintner, J., Tonboe, R.T., Long, D.G. & van Woert, M.L. (2004) Automatic detection and validity of the sea ice edge: An application of enhanced-resolution QuikScat/SeaWinds data. *IEEE Transactions Geoscience and Remote Sensing*, **42**, 1433–1443.
- Hall, D.K., Key, J.R., Casey, K.A., Riggs, G.A. & Cavalieri, D.J. (2004) Sea ice surface temperature product from

- MODIS. *IEEE Transactions Geoscience and Remote Sensing*, **42**, 1076–1087.
- Hendricks, S., Ricker, R. & Helm, V. (2013) *AWI CryoSat-2 sea ice thickness*. From <http://www.meereisportal.de/cryosat>
- Hollands, T. & Dierking, W. (2011) Performance of a multiscale correlation algorithm for the estimation of sea-ice drift from SAR images: initial results. *Annals of Glaciology*, **52**, 311–317.
- Huntemann, M., Heygster, G., Kaleschke, L. et al. (2014) Empirical sea ice thickness retrieval during the freeze-up period from SMOS high incident angle observations. *The Cryosphere*, **8**, 439–451.
- IPCC. (2013) *Climate Change 2013: The Physical Science Basis. Contribution of Working Group I to the Fifth Assessment Report of the Intergovernmental Panel on Climate Change* (Eds. T. Stocker et al.) Cambridge University Press, Cambridge, UK.
- Istomina, L., Heygster, G., Huntemann, M. et al. (2015) Melt pond fraction and spectral sea ice albedo retrieval from MERIS data – Part 2: Case studies and trends of sea ice albedo and melt ponds in the Arctic for years 2002–2011. *The Cryosphere*, **9**, 1567–1578.
- Ivanova, N., Johannessen, O.M., Pedersen, L.T. & Tonboe, R.T. (2014) Retrieval of Arctic sea ice parameters by satellite passive microwave sensors: a comparison between eleven sea ice algorithms. *IEEE Transactions Geoscience and Remote Sensing*, **52**, 7233–7246.
- Jackson, C. R. & Apel, J. R. (Eds.) (2004). *Synthetic Aperture Radar Marine User's Manual*. National Oceanic and Atmospheric Administration, US Dept. of Commerce, Washington, DC, USA.
- Kaleschke, L., Lüpkes, C., Vihma, T. et al. (2001) SSM/I Sea ice remote sensing for mesoscale ocean-atmosphere interaction analysis. *Canadian Journal of Remote Sensing*, **27**, 526–537.
- Kaleschke, L., Maaß, N., Haas, C., Hendricks, S., Heygster, G. & Tonboe, R.T. (2010) A sea ice thickness retrieval model for 1.4 GHz radiometry and application to airborne measurements over low salinity sea ice. *The Cryosphere*, **4**, 583–592.
- Kern, S., & Spreen, G. (2015) Uncertainties in Antarctic sea-ice thickness retrieval from ICESat. *Annals of Glaciology*, **56**, 107–119.
- Kern, S., Ozsoy-Cicek, B., Willmes, S., Nicolaus, M., Haas, C. & Ackley, S. (2011) An intercomparison between AMSR-E snow-depth and satellite C- and Ku-band radar backscatter data for Antarctic sea ice. *Annals of Glaciology*, **52**, 279–290.
- Key, J. & Haeffliger, M. (1992) Arctic ice surface temperature retrieval from AHVRR thermal channels. *Journal of Geophysical Research*, **97**(D5), 5885–5893.
- Komarov, A. & Barber, D. (2014) Sea Ice Motion Tracking from Sequential Dual-Polarization RADARSAT-2 Images. *IEEE Transactions Geoscience and Remote Sensing*, **52**, 121–136.
- Kurtz, N.T., Farrell, S.L., Studinger, M. et al. (2013) Sea ice thickness, freeboard, and snow depth products from Operation IceBridge airborne data. *The Cryosphere*, **7**, 1035–1056.
- Kurtz, N. T., Galin, N. & Studinger, M. (2014) An improved CryoSat-2 sea ice freeboard retrieval algorithm through the use of waveform fitting. *The Cryosphere*, **8**, 1217–1237.
- Kwok, R. (2004) Annual cycles of multiyear sea ice coverage of the Arctic Ocean: 1999–2003. *Journal of Geophysical Research*, **109**, C11004.
- Kwok, R. (2006) Contrasts in sea ice deformation and production in the Arctic seasonal and perennial ice zones. *Journal of Geophysical Research*, **111**, C11S22.
- Kwok, R. (2008) Summer sea ice motion from the 18 GHz channel of AMSR-E and the exchange of sea ice between the Pacific and Atlantic sectors. *Geophysical Research Letters*, **35**, L03504.
- Kwok, R. & Cunningham, G.F. (2008) ICESat over Arctic sea ice: Estimation of snow depth and ice thickness. *Journal of Geophysical Research*, **113**, C08010.
- Kwok, R. & Cunningham, G.F. (2015) Variability of Arctic sea ice thickness and volume from CryoSat-2. *Philosophical Transactions of the Royal Society A*, **373**(2045).
- Kwok, R., Nghiem, S.V., Yueh, S.H. & Huynh, D.D. (1995) Retrieval of thin ice thickness from multifrequency polarimetric SAR data. *Remote Sensing of Environment*, **51**, 361–374.
- Kwok, R., Schweiger, A., Rothrock, D.A., Pang, S. & Kottmeier, C. (1998) Sea ice motion from satellite passive microwave imagery assessed with ERS SAR and buoy motions. *Journal of Geophysical Research*, **103**, 8191–8214.
- Kwok, R., Cunningham, G.F., Wensnahan, M., Rigor, I., Zwally, H.J. & Yi, D. (2009) Thinning and volume loss of the Arctic Ocean sea ice cover: 2003–2008. *Journal of Geophysical Research*, **114**, C07005.
- Kwok, R., Curlander, J., McConnel, R. & Pang, S.S. (1990) An ice-motion tracking system at the Alaska SAR Facility. *IEEE J. Oceanic Engineering*, **15**, 44–54.
- Lange, M.A. & Eicken, H. (1981) Textural characteristics of sea ice and the major mechanisms of ice growth in the Weddell Sea. *Annals of Glaciology*, **15**, 210–215.
- Lavergne, T., Eastwood, S., Teffah, Z., Schyberg, H. & Breivik, L.-A. (2010) Sea ice motion from low-resolution satellite sensors: An alternative method and its validation in the Arctic. *Journal of Geophysical Research*, **115**, C10032.
- Laxon, S.W., Giles, K.A., Ridout, A.L. et al. (2013) CryoSat-2 estimates of Arctic sea ice thickness and volume. *Geophysical Research Letters*, **40**, 1–6.
- Laxon, S., Peacock, N. & Smith, D. (2003) High interannual variability of sea ice thickness in the Arctic region. *Nature*, **425**, 947–950.
- Lindell, D.B. & Long, D.G. (2016) Multiyear Arctic sea ice classification using OSCAT and QuikSCAT. *IEEE Transactions on Geoscience and Remote Sensing*, **54**, 167–175.
- Lubin, D. & Massom, R.A. (2006) *Polar Remote Sensing. Volume 1: Atmosphere & Polar Oceans*. Praxis/Springer.
- Maaß, N., Kaleschke, L., Tian-Kunze, X. & Drusch, M. (2013) Snow thickness retrieval over thick Arctic sea ice using SMOS satellite data. *The Cryosphere*, **7**, 1971–1989.
- Markus, T. & Cavalieri, D.J. (1998) Snow depth distribution over sea ice in the Southern Ocean from satellite passive

- microwave data. In: *Antarctic Sea Ice: Physical Processes, Interactions, and Variability*. Antarctic Research Series (Ed. M.O. Jeffries). American Geophysical Union. Antarctic Research Series, **74**, 19–39.
- Markus, T. & Cavalieri, D.J. (2000). An enhancement of the NASA Team sea ice algorithm. *IEEE Transactions Geoscience and Remote Sensing*, **38**, 1387–1398.
- Markus, T., Cavalieri, D.J., Tschudi, M.A. & Ivanoff, A. (2003) Comparison of aerial video and Landsat 7 data over ponded sea ice. *Remote Sensing of Environment*, **86**, 458–469.
- Markus, T., Stroeve, J.C. & Miller, J. (2009) Recent changes in Arctic sea ice melt onset, freezeup, and melt season length. *Journal of Geophysical Research*, **114**, C12024.
- Martin, S., Drucker, R., Kwok, R. & Holt, B. (2004) Estimation of the thin ice thickness and heat flux for the Chukchi Sea Alaskan coast polynya from Special Sensor Microwave/Imager data, 1990–2001. *Journal of Geophysical Research*, **109**(C10), C10012.
- Martin, S., Drucker, R., Kwok, R. & Holt, B. (2005) Improvements in the estimates of ice thickness and production in the Chukchi Sea polynyas derived from AMSR-E. *Geophysical Research Letters*, **32**, L05505.
- Meier, W.N., Gallaher, D. & Campbell, G.G. (2013) New estimates of Arctic and Antarctic sea ice extent during September 1964 from recovered Nimbus I satellite imagery. *The Cryosphere*, **7**, 699–705.
- Moen, M.-A. N., Doulgeris, A.P., Anfinsen, S.N. et al. (2013) Comparison of feature based segmentation of full polarimetric SAR satellite sea ice images with manually drawn ice charts. *The Cryosphere*, **7**, 1693–1705.
- Nakamura, K., Wakabayashi, H., Naoki, K., Nishio, F., Moriyama, T. & Uratsuka, S. (2005) Observation of Sea-Ice Thickness in the Sea of Okhotsk by Using Dual-Frequency and Fully Polarimetric Airborne SAR (Pi-SAR) Data. *IEEE Transactions Geoscience and Remote Sensing*, **43**, 2460–2469.
- Nakamura, K., Wakabayashi, H., Uto, S., Ushio, S. & Nishio, F. (2009). Observation of Sea-Ice Thickness Using ENVISAT Data From Lützow-Holm Bay, East Antarctica. *IEEE Transactions Geoscience and Remote Sensing Letters*, **6**, 277–281.
- Nihashi, S., Ohshima, K.I., Tamura, T., Fukamachi, Y. & Saitoh, S. (2009) Thickness and production of sea ice in the Okhotsk Sea coastal polynyas from AMSR-E. *Journal of Geophysical Research*, **114**, C10025.
- Ochilov, S. & Clausi, D. (2012) Operational SAR Sea-Ice Image Classification. *IEEE Transactions Geoscience and Remote Sensing*, **50**, 4397–4408.
- Onstott, R.G. & Shuchman, R.A. (2004) SAR Measurement of Sea Ice. In: *Synthetic Aperture Radar Marine User's Manual* (Eds. C.R. Jackson & J.R. Apel), pp. 81–115. National Oceanic and Atmospheric Administration, US Dept. of Commerce, Washington, DC, USA.
- Ozsoy-Cicek, B., Ackley, S.F., Worby, A., Xie, H. & Lieser, J. (2011) Antarctic sea-ice extents and concentrations: comparison of satellite and ship measurements from International Polar Year cruises. *Annals of Glaciology*, **52**, 318–326.
- Parkinson, C. L. (2014) Global sea ice coverage from satellite data: Annual cycle and 35-yr trends. *Journal of Climate*, **27**, 9377–9382.
- Perovich, D.K. & Polashenski, C. (2012) Albedo evolution of seasonal Arctic sea ice. *Geophysical Research Letters*, **39**, L08501.
- Perovich, D.K., Tucker III, W.B. & Ligett, K.A. (2002) Aerial observations of the evolution of ice surface conditions during summer. *Journal of Geophysical Research*, **107**, 8048.
- Petrelli, P., Bindoff, N.L. & Bergamasco, A. (2008) The sea ice dynamics of Terra Nova Bay and Ross Ice Shelf polynyas during a spring and winter simulation. *Journal of Geophysical Research*, **113**, C09003.
- Rees, W.G. & James, S.P. (1992) Angular variation of the infrared emissivity of ice and water surfaces. *International Journal of Remote Sensing*, **13**, 2873–2886.
- Remund, Q.P. & Long, D.G. (1999) Sea ice extent mapping using Ku-band scatterometer data. *Journal of Geophysical Research*, **104**, 11 515–11 527.
- Ricker, R., Hendricks, S., Helm, V., Skourup, H. & Davidson, M. (2014) Sensitivity of CryoSat-2 Arctic sea-ice freeboard and thickness on radar-waveform interpretation. *The Cryosphere*, **8**, 1607–1622.
- Ricker, R., Hendricks, S., Perovich, D.K., Helm, V. & Gerdes, R. (2015) Impact of snow accumulation on CryoSat-2 range retrievals over Arctic sea ice: An observational approach with buoy data. *Geophysical Research Letters*, **42**, 4447–4455.
- Rivas, M.B., Verspeek, J., Verhoef, A. & Stoffelen, A. (2012) Bayesian sea ice detection with the advanced scatterometer ASCAT. *IEEE Transactions Geoscience and Remote Sensing*, **50**, 2649–2657.
- Rösel, A. & Kaleschke, L. (2012) Exceptional melt pond occurrence in the years 2007 and 2011 on the Arctic sea ice revealed from MODIS satellite data. *Journal of Geophysical Research*, **117**(C5), C05018.
- Rösel, A., Kaleschke, L. & Birnbaum, G. (2012) Melt ponds on Arctic sea ice determined from MODIS satellite data using an artificial neural network. *The Cryosphere*, **6**, 431–446.
- Smith, D.M. (1996) Extraction of winter total sea-ice concentration in the Greenland and Barents Seas from SSM/I data. *International Journal of Remote Sensing*, **17**, 2625–2646.
- Spren, G., Kaleschke, L. & Heygster, G. (2008) Sea ice remote sensing using AMSR-E 89-GHz channels. *Journal of Geophysical Research*, **113**, C02S03.
- Sumata, H., Lavergne, T., Girard-Ardhuin, F. et al. (2014) An Intercomparison of ice drift products in the Arctic Ocean for 2002–2006. *Journal of Geophysical Research*, **119**, 4887–4921.
- Tamura, T. & Ohshima, K.I. (2011) Mapping of sea ice production in the Arctic coastal polynyas. *Journal of Geophysical Research*, **116**, C07030.
- Tamura, T., Ohshima, K.I. & Nihashi, S. (2008) Mapping of sea ice production for Antarctic coastal polynyas. *Geophysical Research Letters*, **35**, L07606.



- Tian-Kunze, X., Kaleschke, L., Maaß, N., Mäkynen, M., Serra, N. & Drusch, M. (2013) SMOS-derived thin sea ice thickness: algorithm baseline, product specifications and initial verification. *The Cryosphere*, **8**, 997–1018.
- Tilling, R. L., Ridout, A., Shepherd, A. & Wingham, D. J. (2015) Increased Arctic sea ice volume after anomalously low melting in 2013. *Nature Geoscience*, **8**, 643–646.
- Tschudi, M.A., Maslanik, J.A. & Perovich, D.K. (2008) Derivation of melt pond coverage on Arctic sea ice using MODIS observations. *Remote Sensing of Environment*, **112**, 2605–2614.
- Ulaby, F.T., Moore, R.K. & Fung, A.K. (1982) *Microwave Remote Sensing, Active and Passive*. Volume II: Radar Remote Sensing and Surface Scattering and Emission Theory. Addison Wesley Publishing, London.
- Ulaby, F.T., Moore, R.K. & Fung, A.K. (1986) *Microwave Remote Sensing, Active and Passive*. Volume III: From Theory to Applications. Addison Wesley Publishing, London.
- Van Woert, M.L. (1999) Wintertime dynamics of Terra Nova Bay polynya. *Journal of Geophysical Research*, **104**, 7753–7769.
- Wadhams, P. (2000) *Ice in the Ocean*. Gordon and Breach Science Publisher, London.
- Willatt, R.C., Giles, K.A., Laxon, S.W., Stone-Drake, L. & Worby, A.P. (2010) Field investigations of Ku-band radar penetration into snow cover on Antarctic sea ice. *IEEE Transactions on Geoscience and Remote Sensing*, **48**, 365–372.
- Willmes, S. & Heinemann, G. (2015) Pan-Arctic lead detection from MODIS thermal infrared imagery. *Annals of Glaciology*, **56**, 29–37.
- Willmes, S. & Heinemann, G. (2016) Sea-ice wintertime lead frequencies and regional characteristics in the Arctic, 2003–2015. *Remote Sensing*, **8**, 4.
- Willmes, S., Adams, S., Schröder, D. & Heinemann, G. (2011) Spatio-temporal variability of polynya dynamics and ice production in the Laptev Sea between winters of 1979/80 and 2007/08. *Polar Research*, **30**, 5971.
- Willmes, S., Haas, C., Nicolaus, M. & Bareiss, J. (2009) Satellite microwave observations of the interannual variability of snowmelt on sea ice in the Southern Ocean. *Journal of Geophysical Research*, **114**, C03006.
- Worby, A.P., Markus, T., Steer, A.D., Lytle, V.I. & Massom, R.A. (2008) Evaluation of AMSR-E snow depth product over East Antarctic sea ice using in situ measurements and aerial photography. *Journal of Geophysical Research*, **113**, C05S94.
- Yu, Y. & Rothrock, D. A. (1996). Thin ice thickness from satellite thermal imagery. *Journal of Geophysical Research*, **101**, 25753–25766.
- Yu, Y. & Lindsay, R.W. (2003) Comparison of thin ice thickness distributions derived from RADARSAT Geophysical Processor System and advanced very high resolution radiometer data sets. *Journal of Geophysical Research*, **108**, 3387.
- Zwally, H.J., Schutz, B.E., Abdalati, W. et al. (2002) ICESat's laser measurements of polar ice, atmosphere, ocean, and land. *Journal of Geodynamics*, **34**, 405–445.
- Zygmuntowska, M., Khvorostovsky, K., Helm, V. & Sandven, S. (2013) Waveform classification of airborne synthetic aperture radar altimeter over Arctic sea ice. *The Cryosphere*, **7**, 1315–1324.